



Atmospheric circulation and hydroclimate impacts of alternative warming scenarios for the Eocene

Henrik Carlson¹ and Rodrigo Caballero¹

¹Department of Meteorology, Stockholm University

Correspondence to: Henrik Carlson (henrik@misu.su.se)

Abstract. Recent work in modelling the warm climates of the Early Eocene shows that it is possible to obtain a reasonable global match between model surface temperature and proxy reconstructions, but only by using extremely high atmospheric CO₂ concentrations or more modest CO₂ levels complemented by a reduction in global cloud albedo. Understanding the mix of radiative forcing that gave rise to Eocene warmth has important implications for constraining Earth's climate sensitivity, but progress in this direction is hampered by the lack of direct proxy constraints on cloud properties. Here, we explore the potential for distinguishing among different radiative forcing scenarios via their impact on regional climate changes. We do this by comparing climate model simulations of two end-member scenarios: one in which the climate is warmed entirely by CO₂, and another in which it is warmed entirely by reduced cloud albedo (which we refer to as the “low CO₂-thin clouds” or LCTC scenario). The two simulations have almost identical global-mean surface temperature and equator-to-pole temperature difference, but the LCTC scenario has ~11% greater global-mean precipitation. The LCTC simulation also has cooler midlatitude continents and warmer oceans than the high-CO₂ scenario, and a tropical climate which is significantly more El Niño-like. We discuss the potential implications of these regional changes for terrestrial hydroclimate and vegetation.

1 Introduction

The Early Eocene (~50 Ma) was characterized by very warm surface temperatures compared with the present day (Huber, 2008; Pagani et al., 2014). Considerable progress has been made recently in reconciling proxy temperature reconstructions with climate model simulations of this period: models can now capture both the reconstructed global-mean and equator-pole temperature difference with much greater fidelity than before (Huber and Caballero, 2011; Lunt et al., 2012; Kiehl and Shields, 2013). A remaining problem is to understand what combination of radiative forcing and climate sensitivity gave rise to these very elevated temperatures in the first place (Caballero and Huber, 2013). While early Cenozoic CO₂ concentrations are understood to have been higher than modern (Royer, 2014), achieving a good match with reconstructed temperatures using CO₂ alone as the warming agent requires extremely high model CO₂ levels (Lunt et al., 2012), exceeding even the rather loose constraints imposed by the CO₂ proxies.

Non-CO₂ greenhouse gases such as methane and nitrous oxide may have contributed some of the warming (Beerling et al., 2011), but we lack suitable proxies to constrain their concentrations. Another hypothesis is that reduced aerosol loading during the Eocene could play an important role, particularly via its effect on cloud properties (Kump and Pollard, 2008; Kiehl and



Shields, 2013). Reduced abundance of aerosols and thus of cloud condensation nuclei is generally thought to lead to larger cloud droplets and reduced cloud albedo (Lohmann and Feichter, 2005). A global reduction in aerosol loading would thus lead to lower planetary albedo and a warmer climate. However we again lack proxies to constrain paleo-aerosol abundances, and cloud-aerosol interactions themselves are still imperfectly understood (Stevens and Feingold, 2009), so this scenario remains speculative. Nonetheless, the problem of disentangling the mix of radiative forcing agents that gave rise to Eocene warmth remains of crucial importance given its implications for climate sensitivity and thus predictions of future climate change (Caballero and Huber, 2013).

Here, we explore the potential for constraining the radiative forcing mix responsible for Eocene warmth *indirectly*—that is, without relying on direct proxies for aerosols or non-CO₂ greenhouse gases. Different combinations of forcing agents supporting the same global-mean surface temperature may leave different signatures in other climatological fields that are potentially detectable in the geological record. We focus specifically on the distinction between warming by greenhouse gases—which affect the longwave radiation—and warming by reduced cloud albedo, which affects solar radiation. We do this by comparing simulations of the Eocene climate warmed solely by increased CO₂ with simulations with lower CO₂ warmed solely by reduced cloud albedo, but with indistinguishable global-mean surface temperatures. As in previous work (Kump and Pollard, 2008; Kiehl and Shields, 2013) we reduce cloud albedo by globally increasing the prescribed size of cloud droplets; we refer to these as “low CO₂–thin clouds” (LCTC) simulations (because the clouds are optically thinner in the shortwave spectrum). We pay particular attention to the hydrological cycle, which is known to respond differently to warming by longwave and shortwave forcing (O’Gorman et al., 2012). A similar discussion arises in the context of geoengineering proposals to artificially increase Earth’s planetary albedo in order to offset some of the warming due to anthropogenic CO₂ emissions; it is well known that the resulting climate has a significantly different hydrological cycle compared with a climate subject to the same net radiative forcing but due to a more modest increase in CO₂ (McNutt et al., 2015). Differences in hydrological regime could potentially be detectable in the terrestrial record, particularly in vegetation patterns.

Our modelling approach is further described in Section 2. Section 3 presents an overview of the climatology in the control simulation and its changes in the LCTC case. Section 4 discusses the global-mean change in precipitation and its relation to energetic constraints. Regional climate differences between the two simulations and their relation to circulation changes are discussed in Section 5, while changes in terrestrial hydroclimate are discussed in Section 6. Finally, Section 7 summarizes our conclusions.

2 Methods

2.1 Model and simulations

We employ the Community Atmospheric Model 3.1 (CAM3) developed by the National Center for Atmospheric research (NCAR) (Collins et al., 2006) at T42 resolution coupled to slab ocean. Ocean heat transport is approximated through a prescribed seasonally-varying energy convergence field (“q-flux”) derived from a fully-coupled Eocene simulation run to equilibrium for a corresponding climate (Huber and Caballero, 2011). The model is configured with Eocene geography and land



surface cover as described in Sewall et al. (2000). Simulation climatologies are computed from 30 years of monthly output obtained after the model has reached equilibrium.

We focus on two end-member simulations of the Eocene: a control run warmed only by increasing CO₂ and an extreme LCTC run warmed only by decreasing the planetary albedo. In the control simulation CO₂ is set to 4480 ppm and the cloud droplet radius takes its default value (8 μm over land and 14 μm over ocean). Various aspects of this simulation have been previously described in Caballero and Huber (2010) and Caballero and Huber (2013). In the LCTC simulation, CO₂ takes its pre-industrial value of 280 ppm while cloud droplet radius is increased by multiplying the default values by a uniform factor of 2.5, yielding 20 μm over land and 35 μm over ocean. Note that this retains the difference between land and ocean values, differently from Kiehl and Shields (2013) who used a single cloud droplet radius globally. There is little knowledge about the actual aerosol concentration during the Eocene, but present-day observations in remote regions indicate a land-sea difference in droplet size can be expected even in the absence of anthropogenic emissions (Bréon and Colzy, 2000).

These are very large and likely unrealistic droplet sizes, chosen simply because they lead to the same global-mean surface temperature as in the control run. Our intention is to compare two end-member states which maximise the difference between the two warming agents. Intermediate combinations of CO₂ and cloud albedo (e.g. Kiehl and Shields, 2013) will presumably have intermediate climate impacts; to test this hypothesis, we also conducted a third simulation where CO₂ is set to 1120 ppm and droplet radii are scaled by a factor of 1.6, and confirmed that the resulting climate differs from the control in a qualitatively similar way as described below for the extreme LCTC case, but with smaller overall amplitudes. In the interest of conciseness we focus here only on the end-member cases.

2.2 Potential evapotranspiration and aridity index

To estimate terrestrial hydroclimate impacts in Section 6 we use the standard aridity index P/PET , where P is precipitation and PET is potential evapotranspiration (Middleton and Thomas, 1997). PET is estimated using the Penman-Monteith equation

$$PET = \frac{\Delta(R_n - G) + \rho_a c_p e_s (1 - RH) C_H U}{L_v (\Delta + \gamma (1 + r_s C_H U))}, \quad (1)$$

where ρ_a is the density of air, c_p is the specific heat capacity of air, e_s is the saturation water vapor pressure at temperature T , RH is relative humidity, C_H is a bulk transfer coefficient, U is 10-meter wind, L_v is the latent heat of water, r_s is bulk stomatal resistance and $\Delta = 4098 e_s / (237.3 + T)^2$, where T is the 2-meter temperature. The difference between the net downward radiation R_n and heat flux into the ground G is approximated as $R_n - G = SH + LH$, where SH is the sensible heat flux and LH is the latent heat flux. Finally, $\gamma = c_p p_s / \epsilon L_v$ where p_s is the surface pressure and $\epsilon = 0.622$. The same estimate of PET is described in further detail in Scheff and Frierson (2014) and closely follows Allen et al. (2005).

We compute PET from monthly-mean model output, which is shown by previous studies to give a good representation of PET in the modern day climate (Feng and Fu, 2013), though some error is incurred by not resolving higher frequency variability. More specifically, if warming causes a large change in the relation between day and night temperatures then the calculation of PET using monthly values is not exact (Scheff and Frierson, 2014). Following previous work (Feng and Fu, 2013) we use a constant value $r_s = 70 \text{ s m}^{-1}$. As discussed in Section 6 this is an important limitation since changes in CO₂



may affect stomatal aperture and thus r_s , with potentially important consequences for terrestrial hydrology (e.g. Betts et al., 2007).

3 Climatologies

This section describes the main climatological features of the two simulations, to be further analysed and interpreted in subsequent sections. Annual-mean surface temperature and precipitation fields in our control case (Figure 2a,c) agree closely with those in the corresponding fully-coupled simulations of Huber and Caballero (2011); as discussed in that paper, the modelled temperature field reproduces the available proxy temperature reasonably well, with no appreciable bias in either the global-mean temperature or the mean equator-pole temperature difference. As shown in Carmichael et al. (2015) (where this simulation is referred to as CCSM_H-16x), the precipitation field is also in broad agreement with a global compilation of precipitation proxies, albeit with some mismatches particularly in the Southern Hemisphere high latitudes. This provides confidence that at least the control simulation is a reasonable approximation to the Eocene climate.

Zonal- and annual-mean profiles of surface temperature and precipitation for the two simulations are presented in Figure 1. Despite their very different radiative forcing agents, the two simulations have almost identical zonal-mean temperatures, with differences of a few tenths of a degree (in the global mean, the LCTC simulation is cooler by 0.3 K than the control simulation). Precipitation, on the other hand, is significantly larger in the LCTC case, especially in the tropics and in the subtropical flanks of the major midlatitude precipitation zones.

As shown in Figure 2b, however, regional differences in surface temperature are large. Land areas are cooler in the LCTC run by up to 5 K, particularly in subtropical regions with little cloud cover (Figure 2e). Offsetting warming develops over the oceans, notably in twin horseshoe-shaped regions of the Pacific in both hemispheres. These temperature responses are accompanied by large changes in the low-level circulation (Figure 2b). The LCTC case exhibits a cyclonic anomaly over the northern Pacific, with a similar but weaker response over the southern Pacific. The cyclonic anomaly acts to weaken the prevailing subtropical cyclones seen in the control case (Figure 2a). This is reminiscent of the weakening of the subtropical anticyclones seen in the transition from summer to winter in the modern day, which is also accompanied by a cooling of the continents relative to the oceans.

While global-mean temperature is essentially identical in the two simulations, global-mean precipitation is 0.43 mm day^{-1} or about 11% higher in the LCTC case. This must be considered a substantial increase: Carmichael et al. (2015, their Figure 2c) show a robust linear scaling of precipitation with temperature of around $0.06 \text{ mm day}^{-1} \text{ K}^{-1}$, implying that a precipitation increase of this magnitude would require a CO_2 -driven warming in excess of 7 K (comparable to that across the Paleocene-Eocene Thermal Maximum (PETM) hyperthermal event, see Pagani et al., 2014). Moreover, the spatial distribution of the precipitation change is highly non-uniform, with regional increases well in excess of 100%. The greatest precipitation increase is concentrated in the central and eastern equatorial Pacific, partly offset by a large decrease in the western Pacific Warm Pool region. Precipitation also increases across large swaths of the subtropical to midlatitude Pacific and Atlantic Oceans and adjacent land areas.



Cloud cover in the control simulation (Figure 2e) shows broad-scale structures similar to the modern day, with abundant cloud cover over the Pacific Warm Pool and intertropical convergence zones (ITCZ) and over the midlatitude oceanic storm tracks and extensive stratocumulus decks in the eastern subtropical margins of the main ocean basins. Though our LCTC simulation only prescribes changes in cloud droplet size, the resulting dynamical and thermodynamical changes lead to changes also in cloud abundance (Figure 2f). In particular, there is a substantial decrease in cloud fraction in the North Pacific subtropics—
5 in the same region showing a large sea-surface temperature (SST) warming (Figure 2b)—and increased cloud cover over southwestern North America, associated with increased precipitation there (Figure 2d).

Finally, we examine the atmospheric jets and storm tracks in the two simulations (Figures 2g,h). As in the modern climate, zonal winds in the Northern Hemisphere of the control simulation are concentrated into separate jet streams spanning the Pacific and Atlantic basins; differently from modern, the Pacific jet exhibits a marked meridional tilt. The jets are associated with regions of enhanced eddy variability—storm tracks—which are grossly identified here by the sub-monthly eddy kinetic energy $EKE = (u'^2 + v'^2)/2$, where u and v are zonal and meridional components of the wind and primes denote sub-monthly deviations from monthly climatology. Lower-tropospheric jets and storm tracks are intimately connected via wave-mean flow interaction (Shaw et al., 2016). In the control run, the North Pacific storm track is further northward than observed in the modern climate (Shaw et al., 2016), consistent with the meridional tilt of the jet. In the LCTC case, however, the North Pacific
15 jet and storm track show a marked equatorward shift, with enhanced winds and EKE in the subtropical basin and reductions further north. In the Southern Hemisphere the jet and storm tracks are more zonally continuous, but a similar equatorward shift can be observed in the LCTC case. Along the equator, the LCTC case shows a low-level westerly wind anomaly in the western Pacific, consistent with a weakening of the Walker Cell and an eastward shift of precipitation towards the central Pacific as
20 noted above. There is also a marked reduction in EKE in the western equatorial Pacific, in the same region where precipitation decreases. Much of the sub-seasonal variability in the tropics is due to the Madden-Julian Oscillation (MJO). As discussed elsewhere (Caballero and Huber, 2010; Arnold et al., 2014; Carlson and Caballero, 2016), warm climates show a strongly enhanced MJO in a range of climate models including the one used here. It is possible that the MJO is more muted in the LCTC simulation, perhaps because of changes in the Walker Cell, but we do not investigate this issue further here.

25 4 Global-mean precipitation and energetic constraints

As noted above, global-mean precipitation in the LCTC case is around 11% higher than in the control. A precipitation increase in response to a simultaneous drop in CO_2 and planetary albedo is consistent with simulations of geoengineering scenarios, where increased CO_2 and planetary albedo lead to lower precipitation (Bala et al., 2008). In this section we account for the global-mean precipitation change in our simulations from the perspective of energy budget constraints (O’Gorman et al., 2012).

30 The global-mean atmospheric energy budget can be written, assuming steady state, as

$$SW_{TOA} - SW_{srf} + LW_{TOA} - LW_{srf} - LH - SH = 0, \quad (2)$$

where SW and LW refer to shortwave and longwave radiation with subscripts TOA and srf indicating top-of-atmosphere and surface fluxes respectively, while LH and SH are surface latent and sensible heat fluxes respectively. All fluxes are taken



to be positive downwards. Given the atmospheric steady state assumption, $LH = L_v P$, where P is global-mean precipitation and L_v the latent heat capacity. If the planet as a whole is also in steady state, then $SW_{TOA} + LW_{TOA} = 0$ and (2) reduces to the surface energy budget

$$SW_{srf} + LW_{srf} + LH + SH = 0. \quad (3)$$

5 For climates in planetary energy balance, like those studied here, the atmospheric and surface energy budgets are thus equivalent, and provide alternative and complementary perspectives on the mechanisms controlling changes in precipitation (Allen and Ingram, 2002; Pierrehumbert, 2002). We examine both perspectives here.

The terms in (2) for the control case are shown in Figure 3a. Atmospheric heating is dominated by the LH component, but shortwave absorption ($SW_{TOA} - SW_{srf}$) also makes a large contribution as can be expected in this very warm and thus
10 moist climate. Sensible heating makes a much smaller contribution. The heating is entirely balanced by net longwave cooling ($LW_{TOA} - LW_{srf}$). Changes when going to the LCTC case are shown in Figure 3b. Net longwave cooling increases by about 17 W m^{-2} in the LCTC run. This increased cooling is a combination of clear-sky and cloud effects. In clear skies, lowering CO_2 while keeping temperature and humidity fixed yields stronger outgoing longwave radiation at the TOA (which increases atmospheric cooling) and weaker downward radiation at the surface (which decreases cooling). The former effect dominates
15 the latter, however (Pendergrass and Hartmann, 2014), so the net result is increased cooling. The contribution of cloud effects can be estimated using the cloud radiative effect (CRE, difference between all-sky and clear-sky radiation). Net atmospheric longwave CRE—the difference between TOA and surface CRE—is about 13 W m^{-2} in the control case, implying clouds have a net heating effect in the longwave. This heating drops to 7 W m^{-2} in the LCTC case, which means that the general reduction in cloud cover seen in Figure 2f contributes around 6 W m^{-2} compared to the 17 W m^{-2} total increase in atmospheric cooling.
20 Finally, Figure 3b also shows that increased longwave cooling is balanced mostly by latent heating, with sensible heating and shortwave absorption playing minor roles. In summary, the atmospheric energy budget perspective indicates that precipitation increases in the LCTC run to compensate for increased longwave cooling due mostly to the clear-sky effect of reduced CO_2 , with some contribution also from changes in cloud abundance.

From the surface budget perspective (3), Figure 3b (noting the reversed sign convention) shows that increased shortwave
25 heating of the surface in the LCTC case—due to the lower cloud albedo—is mainly compensated through increased latent heat flux and also increased longwave surface cooling (due to reduced downwelling radiation, as noted above). From the surface perspective, then, precipitation increases in the LCTC case mostly to balance increased surface solar heating. This points to a rather different physical picture than the atmospheric perspective, in which shortwave fluxes play a negligible role. Given the equivalence of (2) and (3), the two physical pictures must of course be consistent. A plausible hypothesis for how consistency
30 is achieved runs as follows: atmospheric destabilization by radiative cooling due to reduced CO_2 accelerates convection, increasing rainfall and also mixing drier air down into the boundary layer; this drying increases evaporative demand at the surface, and the extra energy required to maintain surface temperature against evaporative cooling is supplied by increased solar absorption due to reduced cloud albedo. Fully reconciling the two perspectives in a causal, mechanistic way would



require considerably more work going beyond the scope of this paper. However, some evidence supporting this hypothesis is shown in the following section.

5 Atmospheric circulation and regional climate response

While the energetic constraints discussed above help explain the global increase in precipitation in the LCTC case, they place
5 no constraints on its spatial distribution, which is highly heterogeneous (Figure 2d). These regional changes in precipitation are
accompanied by pronounced changes in the surface temperature pattern (Figure 2b) and the atmospheric general circulation
(Figure 2h). In this section we explore how these various changes are interrelated. To do this, it is useful to think of the
transition from the control to the LCTC climate as if it occurred in 3 stages: first CO₂ is reduced instantaneously, producing
10 a fast adjustment in the atmosphere and land before SST has time to change (Sherwood et al., 2015); then cloud albedo is
instantaneously reduced, producing a further fast adjustment; and finally the SST slowly adjusts to its final equilibrium pattern.
Circulation changes linked to the fast adjustments will condition the evolution of the SST pattern, which in turn will affect the
circulation.

We make this conceptual picture quantitative by running 3 fixed-SST experiments. Two employ prescribed (seasonally-
varying) SST from the control run; one uses control values of cloud drop radius while CO₂ is reduced to 280 ppm while the
15 other uses control CO₂ and cloud drop radius increased by a factor of 2.5. The third run uses control values of CO₂ and cloud
drop radius but prescribes the SST from the LCTC case. Comparing these fixed-SST simulations with the control run allows
us to separately quantify the effect of changing CO₂, cloud albedo and SST pattern.

Figure 4 shows the surface temperature and low-level circulation responses in the three simulations. The sum of all changes
(Figure 4d) gives a reasonable match to the full response in the LCTC run (Figure 2b), though with somewhat higher amplitude,
20 suggesting that this linear decomposition is an adequate approximation. The direct response to reduced CO₂ (Figure 4a)
involves strong cooling of the extratropical continents and a basin-scale cyclonic anomaly over both the North and South
Pacific, with westerly anomalies spanning the tropics and lower midlatitudes and easterly anomalies further north. This is
accompanied by an equatorward migration of the upper level jets in both hemispheres, consistently with previous work (Grise
and Polvani, 2013). Cooling of midlatitude land relative to the ocean accompanied by cyclonic anomalies over the ocean is
25 reminiscent of the negative phase of the “cold ocean–warm land” pattern (Wallace et al., 1996). It is also consistent with the
work of Molteni et al. (2011), who show cyclonic anomalies over the North Pacific in simulations with permanently increased
land-ocean temperature contrast and explore alternative dynamical scenarios to account for them.

The direct response to cloud albedo reduction (Figure 4b) is a warming of the continents, particularly at high latitudes. This
warming is highly seasonal, peaking in the summer, unlike the CO₂ response which is more even through the year. Somewhat
30 surprisingly, the circulation response to continental warming is weak and not obviously anticyclonic except in the South Pacific.
The reasons for this weak response are unclear; it is perhaps due to the seasonal and high-latitude nature of the warming, but
we do not explore the issue further here.



Finally, the response to changing SST pattern (Figure 4c) features a strong cyclonic anomaly over the North Pacific—where the SST anomaly is strongest—and a weaker cyclonic anomaly over the South Pacific. In the extratropics of both hemispheres, the circulation responses align with those induced by CO₂ alone, and similarly yield an equatorward shift of the lower-tropospheric jets. There is also a strong response in the tropics, in particular an easterly anomaly in the tropical west Pacific indicating a weakened Walker cell consistent with the substantial warm anomalies in the central Pacific.

Precipitation changes from the control for the 3 runs are presented in Figure 5. The sum of all changes (Figure 5d) again captures the change seen in the full LCTC case (Figure 2d) reasonably well. Global-mean precipitation increases by 0.37 mm day⁻¹ in response to CO₂ alone, by 0.05 mm day⁻¹ in response to cloud albedo alone and decreases slightly in response to SST pattern. Thus, most of the 0.42 mm day⁻¹ increase seen in the LCTC run is due to the direct effect of CO₂. Reduced cloud albedo drives little change in precipitation by itself—instead, as discussed at the end of Section 4, it serves to close the surface energy balance, supplying surface solar heating to offset increased evaporative cooling. While CO₂ drives most of the global-mean precipitation change, its spatial pattern (Figure 5a) shows anomalies concentrated in the eastern Pacific and over the Indo-Pacific warm pool, which is very different from that in the final state (Figure 2d). Changes in SST pattern clearly play a major role in redistributing tropical precipitation into the central Pacific (Figure 5c), consistent with warm SST anomalies there enhancing low-level convergence as is evident in Figure 4c.

Taken together, these results indicate a key role for the SST pattern in mediating the transition from the control to the LCTC climate state. So what gives rise to the SST anomaly? Some insight into this question is provided by the work of Vimont et al. (2001), who argue that a cyclonic circulation anomaly in the extratropical North Pacific will yield an SST “footprint” which has precisely the horseshoe structure we find here (compare their Figure 1 with Figure 2b). This happens because the anomalous surface winds affect surface energy fluxes. This interpretation is supported by Figure 6, which shows the net surface energy flux change from the control to the fixed-SST low CO₂ simulation. The pattern of ocean heating and cooling induced by these surface flux anomalies clearly aligns well with the SST anomaly (Figure 4c). Note in particular that the surface energy flux anomaly will tend to warm the central Pacific relative to the rest of the equatorial zone, driving a shift in precipitation into the central Pacific.

A further important point highlighted by Figure 4c is that the SST anomaly itself produces an extratropical circulation response that superposes constructively on the pre-existing CO₂-induced cyclonic circulation anomaly. Given the generally weak atmospheric response to extratropical SST anomalies (Kushnir et al., 2002), it is most likely that this extratropical circulation response is driven from the tropics, in particular by warm SST anomaly in the central Pacific which—as noted above—promotes large precipitation anomalies there, much like in an El Niño event. Such tropical heating anomalies are known to robustly induce cyclonic circulation anomalies in the extratropical North Pacific (Alexander et al., 2002). Furthermore, it is well known from both observations (Caballero, 2007) and model studies (Tandon et al., 2013) that El Niño events and their associated tropical heating anomalies drive an equatorward shift of the extratropical jets and storm tracks, in agreement with what we find here (Figure 2h).

In summary, the picture that emerges is that the direct effect of reduced CO₂ initially drives a basin-scale cyclonic circulation anomaly in each hemisphere of the Pacific Ocean; this circulation anomaly then drives SST anomalies which reinforce the initial



response to CO₂. The direct response to cloud albedo appears to play a minor role in driving regional climate changes. This picture points to an important limitation of our modelling approach, which uses a slab ocean model. With a dynamic ocean, the westerly wind anomalies along the equator (Figure 6) would likely drive a deepening of the ocean thermocline in the eastern equatorial Pacific, shifting the mean climate towards a more El Niño-like state. This response and its global consequences are an important target for future work using a fully-coupled modelling approach.

6 Terrestrial hydroclimate

The widespread differences in regional temperature and precipitation between the control and LCTC runs discussed above have potentially large implications for terrestrial hydroclimate which could be detectable in the geological record, particularly through their impact on vegetation. We address this issue here from the perspective of the aridity index P/PET , where P is precipitation and PET potential evapotranspiration as defined in Section 2.2. While this index has been widely used to study hydroclimate changes in future climates (e.g. Fu and Feng, 2014; Scheff and Frierson, 2015), its limitations are increasingly recognized (Scheff et al., 2017). Notably, its failure to account for changes in stomatal resistance may yield strongly biased results (Milly and Dunne, 2016). Moreover, it is an imperfect indicator of vegetation responses, which also depend on other factors including CO₂ (Roderick et al., 2015). Bearing these caveats in mind, we nonetheless employ P/PET here to provide a rough indication of which terrestrial regions—if any—can be expected to show significant changes in eco-hydrological regime.

Figure 7 shows annual-mean terrestrial precipitation, PET and P/PET fields for the control simulation and differences in the LCTC simulation. In the modern climate, regions with P/PET below 0.65 are classified as dryland, with values below 0.2 classified as arid or hyper-arid. In the control simulation—as in the present day—such regions are concentrated in the subtropics due to a combination of low rainfall and high PET (the latter due to high temperature and high surface insolation because of sparse cloud cover, see Figure 2). The largest P/PET values are found in the high latitudes, where rainfall is greater while temperature and insolation are lower. Note however that high CO₂ levels would promote stomatal closure and increase stomatal resistance, reducing PET and thus raising P/PET values globally (Milly and Dunne, 2016). Moreover, CO₂ fertilization would promote increased vegetation cover (Roderick et al., 2015). Thus the Eocene could have been globally much “greener” than implied by a naive identification of P/PET values in Figure 7e with modern biomes associated the same P/PET .

Turning to the LCTC simulation, Figure 7f shows that the largest changes in P/PET occur in the high latitudes, particularly in northeast Asia and northwest North America. These regions show a large decrease in P/PET , resulting in part from decreased precipitation (especially in northwest North America) but mostly from a substantial increase in PET , most likely driven by increased surface insolation—via the R_n term in (1)—due to reduced cloud albedo. Warm anomalies in northwest North America contribute to increased PET , but counteract it over Antarctica giving a somewhat smaller response there. At the same time, a strong positive P/PET anomaly appears in western North America due to a combination of increased precipitation and reduced PET . We can attribute this north-south drying/wetting dipole across western North America to the equatorward migration of the Pacific stormtrack (Sections 3 and 5), which shifts precipitation southwards, and to the warming-cooling pattern due to the opposing effects of decreasing CO₂ and cloud albedo (Section 5). Another prominent dipole can be seen in



the tropics, with a positive P/PET anomaly in northwestern South America and negative anomalies in southeast Asia. These anomalies are mostly driven by changes in precipitation, associated with the weakening of the Walker Cell.

In the LCTC case, with its lower CO_2 , the caveats discussed above apply in reverse: reduced stomatal resistance will increase PET, dampening positive P/PET anomalies but further enhancing negative anomalies. Low CO_2 will also make it more difficult for vegetation to thrive in regions subject to hydrological stress. We thus expect the northern high latitudes and possibly Antarctica and southeast Asia to be the most promising regions for detectable differences in vegetation in response to our alternative Eocene warming scenarios.

7 Conclusions

We have studied the differences in circulation and hydrological cycle resulting from two extreme scenarios by which Eocene simulations can attain surface temperatures compatible with proxy reconstructions: one by warming exclusively by increased CO_2 (the control case), the other by warming exclusively via reduced cloud albedo (the LCTC case). The two simulations have essentially identical zonal-mean surface temperature, but the LCTC case has significantly higher precipitation. Analysis of the global-mean energy budget (Section 4) suggests that the increased precipitation can be viewed as resulting from greater radiative cooling of the atmosphere in the LCTC case due to its lower CO_2 . The spatial distribution of the precipitation increase is highly heterogeneous, and is concentrated largely in the central equatorial Pacific and in the lower midlatitudes. The midlatitude continents cool in the LCTC simulation, with compensating warming of the oceans particular in horseshoe-shaped patterns in both hemispheres of the Pacific. There are also major changes to the atmospheric circulation, with basin-scale cyclonic anomalies appearing in both hemispheres of the Pacific associated with equatorward shifts of the storm tracks, and a strong weakening of the Walker Cell in the tropics.

More detailed analysis (Section 5) suggests that these various anomalies are dynamically interrelated. Lower CO_2 in the LCTC case leads to continental cooling, which in turn generates cyclonic circulation anomalies over the Pacific. We propose that these cyclonic anomalies in turn leave a horseshoe shaped “footprint” on SSTs via their effect on surface turbulent fluxes (Vimont et al., 2001). This footprint reaches into the central tropical Pacific and promotes increased convection there which, much as in a modern El Niño event, affects the extratropical circulation and enhances the pre-existing cyclonic anomalies. This self-reinforcing mechanism leads to the pronounced regional climate anomalies noted above, which also affect adjacent land areas. Finally, we analysed changes in terrestrial hydroclimate using the simple aridity index P/PET . Paying attention to the caveats inherent in this index, the analysis suggests that the most robust eco-hydrological differences between the two warming scenarios are to be expected in the high latitudes—especially in northwestern North America—and possibly also in tropical southeast Asia.

Our work is intended as an initial exploration, and much work remains to be done to remove the limitations imposed by our choice of a relatively simplified modelling approach. A key limitation is our use of a slab ocean. As noted in Section 5, the ocean will dynamically respond to the westerly surface stress anomalies along the equator (Vimont et al., 2001), possibly leading to a climate state with a permanently reduced tropical thermocline tilt and a more El Niño-like climate. If this were the case, the



ocean dynamical response would in fact further strengthen the tropical anomalies found here, which already resemble an El Niño-like response. Another important caveat is that circulation responses to changes in radiative forcing—and their associated regional climate changes—are sensitive to biases in the unperturbed state (Shepherd, 2014). For example, if the Pacific jet were more zonally oriented in reality than in our control Eocene simulation (Figure 2g), its response in the LCTC scenario could be quite different. A further limitation of our approach is the specification of a uniformly increased cloud drop radius, leaving other aspects of cloud microphysics untouched. This is highly unrealistic in several ways: there is no particular reason to expect that different cloud types would respond in the same way to reduced aerosol loading; moreover, larger cloud drops are expected to coalesce more readily and thus reduce cloud lifetimes, potentially leading to reductions in cloud cover which would be different for different cloud types. In addition, all the above effects would depend on the precise nature and composition of natural aerosol in the Eocene, which remains essentially unknown. Different hypotheses for aerosol composition and cloud microphysics could lead to very different spatial structures of the resulting radiative forcing, with potentially large impacts on the circulation and regional climates.

Despite these important caveats, we conclude that differences in the radiative forcing agent driving Eocene warmth could at least in principle lead to large differences in regional climates leaving potentially detectable traces in the geological record. We have explored here two end-member scenarios, one with very high CO₂ (higher than suggested by current CO₂ proxy reconstructions) and another with pre-industrial CO₂ (which is almost certainly lower than in the Eocene). A more realistic scenario would involve some intermediate mix of warming by CO₂ and by cloud effects (Kiehl and Shields, 2013), which would be expected to yield smaller climate differences than those found here. However, given the large uncertainties discussed above, it remains possible that even an intermediate mix of warming agents could lead to responses as large or larger than those in our study. Future work with a range of models including more complete representations of ocean dynamics and cloud-aerosol interactions is required to settle this question.

Acknowledgements. We thank Qiang Fu, Jack Scheff and Johan Nilsson for useful discussion and comments. The Swedish National Infrastructure for Computing (SNIC) at the National Supercomputing Centre (NSC), Linköping University, provided the high performance computing resources to perform the simulations.



References

- Alexander, M. A., Bladé, I., Newman, M., Lanzante, J. R., Lau, N.-C., and Scott, J. D.: The atmospheric bridge: The influence of ENSO teleconnections on air–sea interaction over the global oceans, *J. Climate*, 15, 2205–2231, 2002.
- Allen, M. R. and Ingram, W. J.: Constraints on future changes in climate and the hydrologic cycle, *Nature*, 419, 224–232, 2002.
- 5 Allen, R. G., Walter, I. A., Elliott, R., Howell, T., Itenfisu, D., and Jensen, M.: ASCE Standardized Reference Evapotranspiration Equation, American Society of Civil Engineers, 59pp, 2005.
- Arnold, N. P., Branson, M., Burt, M. A., Abbot, D. S., Kuang, Z., Randall, D. A., and Tziperman, E.: Effects of explicit atmospheric convection at high CO₂, *Proc. Natl. Acad. Sci. USA*, 111, 10 943–10 948, 2014.
- Bala, G., Duffy, P., and Taylor, K.: Impact of geoengineering schemes on the global hydrological cycle, *Proc. Natl. Acad. Sci. USA*, 105,
10 7664–7669, 2008.
- Beerling, D. J., Fox, A., Stevenson, D. S., and Valdes, P. J.: Enhanced chemistry-climate feedbacks in past greenhouse worlds, *Proc. Natl. Acad. Sci. USA*, 108, 9770–9775, 2011.
- Betts, R. A., Boucher, O., Collins, M., Cox, P. M., Falloon, P. D., Gedney, N., Hemming, D. L., Huntingford, C., Jones, C. D., Sexton, D. M., et al.: Projected increase in continental runoff due to plant responses to increasing carbon dioxide, *Nature*, 448, 1037–1041, 2007.
- 15 Bréon, F.-M. and Colzy, S.: Global distribution of cloud droplet effective radius from POLDER polarization measurements, *Geophys. Res. Lett.*, 27, 4065–4068, 2000.
- Caballero, R.: Role of eddies in the interannual variability of Hadley cell strength, *Geophys. Res. Lett.*, 34, L22 705, 2007.
- Caballero, R. and Huber, M.: Spontaneous transition to superrotation in warm climates simulated by CAM3, *Geophys. Res. Lett.*, 37, L11 701, 2010.
- 20 Caballero, R. and Huber, M.: State-dependent climate sensitivity in past warm climates and its implications for future climate projections, *Proc. Natl. Acad. Sci. USA*, 110, 14 162–14 167, doi:10.1073/pnas.1303365110, <http://dx.doi.org/10.1073/pnas.1303365110>, 2013.
- Carlson, H. and Caballero, R.: Enhanced MJO and transition to superrotation in warm climates, *J. Adv. Model. Earth Syst.*, 8, 304–318, 2016.
- Carmichael, M. J., Lunt, D. J., Huber, M., Heinemann, M., Kiehl, J., LeGrande, A., Loftson, C. A., Roberts, C. D., Sagoo, N., Shields,
25 C., Valdes, P. J., Winguth, A., Winguth, C., and Pancost, R. D.: Insights into the early Eocene hydrological cycle from an ensemble of atmosphere–ocean GCM simulations, *Clim. Past Discuss.*, 11, 3277–3339, 2015.
- Collins, W. D., Rasch, P. J., Boville, B. A., Hack, J. J., McCaa, J. R., Williamson, D. L., Briegleb, B. P., Bitz, C. M., Lin, S.-J., and Zhang, M.: The Formulation and Atmospheric Simulation of the Community Atmosphere Model Version 3 (CAM3), *J. Climate*, 19, 2144–2161, doi:10.1175/JCLI3760.1, <http://dx.doi.org/10.1175/JCLI3760.1>, 2006.
- 30 Feng, S. and Fu, Q.: Expansion of global drylands under a warming climate, *Atmospheric Chemistry and Physics*, 13, 10 081–10 094, doi:10.5194/acp-13-10081-2013, <http://dx.doi.org/10.5194/acp-13-10081-2013>, 2013.
- Fu, Q. and Feng, S.: Responses of terrestrial aridity to global warming, *J. Geophys. Res. Atmos.*, 119, 7863–7875, 2014.
- Grise, K. M. and Polvani, L. M.: Is climate sensitivity related to dynamical sensitivity? A Southern Hemisphere perspective, *Geophys. Res. Lett.*, pp. n/a–n/a, doi:10.1002/2013GL058466, <http://dx.doi.org/10.1002/2013GL058466>, 2013.
- 35 Huber, M.: CLIMATE CHANGE: A Hotter Greenhouse?, *Science*, 321, 353–354, doi:10.1126/science.1161170, <http://dx.doi.org/10.1126/science.1161170>, 2008.



- Huber, M. and Caballero, R.: The early Eocene equable climate problem revisited, *Climate of the Past*, 7, 603–633, doi:10.5194/cp-7-603-2011, <http://dx.doi.org/10.5194/cp-7-603-2011>, 2011.
- Kiehl, J. T. and Shields, C. A.: Sensitivity of the Palaeocene-Eocene Thermal Maximum climate to cloud properties, *Philosophical Transactions of the Royal Society A: Mathematical, Physical and Engineering Sciences*, 371, 20130093–20130093, 2013.
- 5 Kump, L. R. and Pollard, D.: Amplification of Cretaceous Warmth by Biological Cloud Feedbacks, *Science*, 320, 195–195, doi:10.1126/science.1153883, <http://dx.doi.org/10.1126/science.1153883>, 2008.
- Kushnir, Y., Robinson, W., Bladé, I., Hall, N., Peng, S., and Sutton, R.: Atmospheric GCM response to extratropical SST anomalies: Synthesis and evaluation, *J. Climate*, 15, 2233–2256, 2002.
- Lohmann, U. and Feichter, J.: Global indirect aerosol effects: a review, *Atmos. Chem. Phys.*, 5, 715–737, 2005.
- 10 Lunt, D. J., Dunkley Jones, T., Heinemann, M., Huber, M., LeGrande, A., Winguth, A., Loptson, C., Marotzke, J., Roberts, C., Tindall, J., et al.: A model–data comparison for a multi-model ensemble of early Eocene atmosphere–ocean simulations: EoMIP, *Clim. Past*, 8, 1717–1736, 2012.
- McNutt, M. K., Abdalati, W., Caldeira, K., Doney, S. C., Falkowski, P. G., Fetter, S., Fleming, J. R., Hamburg, S. P., Morgan, M. G., Penner, J. E., et al.: *Climate Intervention: Reflecting Sunlight to Cool Earth*, National Academy of Sciences: Washington, DC, USA, 2015.
- 15 Middleton, N. and Thomas, D.: *World atlas of desertification*, Ed. 2, Arnold, Hodder Headline, PLC, 1997.
- Milly, P. C. D. and Dunne, K. A.: Potential evapotranspiration and continental drying, *Nature Clim. Change*, 6, 946–949, 2016.
- Molteni, F., King, M. P., Kucharski, F., and Straus, D. M.: Planetary-scale variability in the northern winter and the impact of land–sea thermal contrast, *Clim. Dyn.*, 37, 151–170, 2011.
- O’Gorman, P. A., Allan, R. P., Byrne, M. P., and Previdi, M.: Energetic constraints on precipitation under climate change, *Surv. Geophys.*, 20 33, 585–608, 2012.
- Pagani, M., Huber, M., and Sageman, B.: Greenhouse climates, in: *Treatise on Geochemistry*, edited by Holland, H. and Turekian, K., pp. 281–304, Elsevier, Oxford, second edn., 2014.
- Pendergrass, A. G. and Hartmann, D. L.: The Atmospheric Energy Constraint on Global-Mean Precipitation Change, *Journal of Climate*, 27, 757–768, 2014.
- 25 Pierrehumbert, R. T.: The hydrologic cycle in deep-time climate problems, *Nature*, 419, 191–198, doi:10.1038/nature01088, <http://dx.doi.org/10.1038/nature01088>, 2002.
- Roderick, M. L., Greve, P., and Farquhar, G. D.: On the assessment of aridity with changes in atmospheric CO₂, *Water Resour. Res.*, 51, 5450–5463, 2015.
- Royer, D.: Atmospheric CO₂ and O₂ during the Phanerozoic: Tools, patterns, and impacts, in: *Treatise on Geochemistry*, edited by Holland, H. and Turekian, K., pp. 251–267, Elsevier, second edition edn., 2014.
- 30 Scheff, J. and Frierson, D. M. W.: Scaling Potential Evapotranspiration with Greenhouse Warming, *J. Climate*, 27, 1539–1558, doi:10.1175/jcli-d-13-00233.1, <http://dx.doi.org/10.1175/JCLI-D-13-00233.1>, 2014.
- Scheff, J. and Frierson, D. M. W.: Terrestrial Aridity and Its Response to Greenhouse Warming across CMIP5 Climate Models, *J. Climate*, 28, 5583–5600, 2015.
- 35 Scheff, J., Seager, R., Liu, H., and Coats, S.: Are glacials dry? Consequences for paleoclimatology and for greenhouse warming, *J. Climate*, p. submitted, 2017.
- Sewall, J. O., Sloan, L. C., Huber, M., and Wing, S.: Climate sensitivity to changes in land surface characteristics, *Global Planet. Change*, 26, 445–465, 2000.



- Shaw, T. A., Baldwin, M., Barnes, E. A., Caballero, R., Garfinkel, C. I., Hwang, Y. T., Li, C., O’Gorman, P. A., Riviere, G., Simpson, I. R., and Voigt, A.: Storm track processes and the opposing influences of climate change, *Nat. Geosci.*, p. doi:10.1038/ngeo2783, 2016.
- Shepherd, T. G.: Atmospheric circulation as a source of uncertainty in climate change projections, *Nat. Geosci.*, 7, 703–708, 2014.
- Sherwood, S. C., Bony, S., Boucher, O., Bretherton, C., Forster, P. M., Gregory, J. M., and Stevens, B.: Adjustments in the forcing-feedback framework for understanding climate change, *Bull. Am. Meteorol. Soc.*, 96, 217–228, 2015.
- 5 Stevens, B. and Feingold, G.: Untangling aerosol effects on clouds and precipitation in a buffered system, *Nature*, 461, 607–613, 2009.
- Tandon, N. F., Gerber, E. P., Sobel, A. H., and Polvani, L. M.: Understanding Hadley cell expansion versus contraction: Insights from simplified models and implications for recent observations, *J. Clim.*, 26, 4304–4321, 2013.
- Vimont, D., Battisti, D., and Hirst, A.: Footprinting: A seasonal connection between the tropics and mid-latitudes, *Geophys. Res. Lett.*, 28, 3923–3926, 2001.
- 10 Wallace, J. M., Zhang, Y., and Bajuk, L.: Interpretation of interdecadal trends in Northern Hemisphere surface air temperature, *J. Climate*, 9, 249–259, 1996.

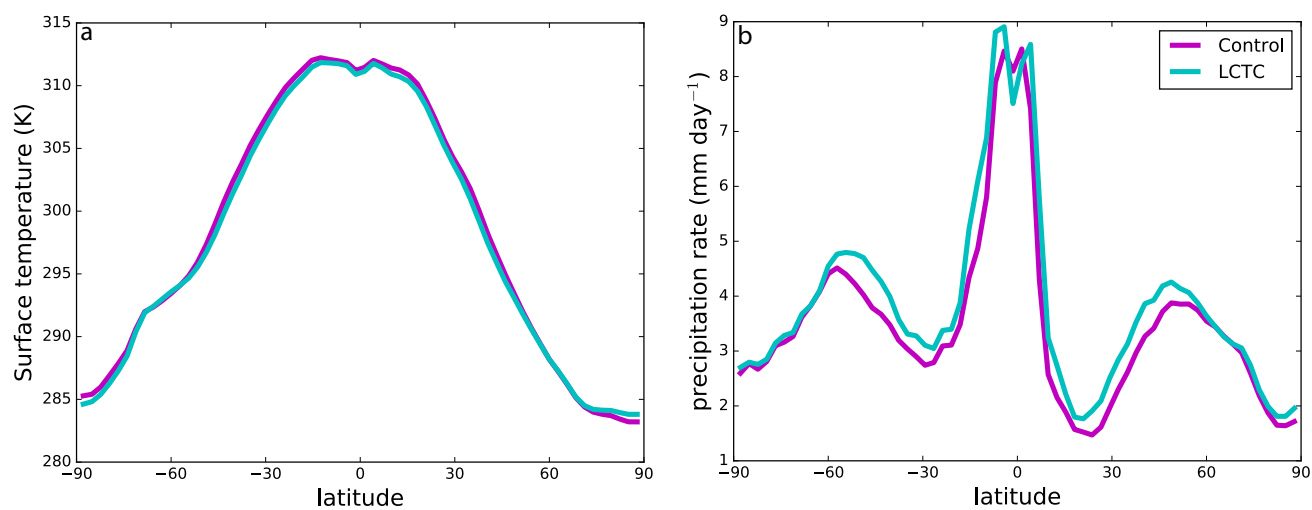


Figure 1. Annual- and zonal-mean surface temperature (a) and precipitation (b) in the control case (magenta) and LCTC case (cyan).

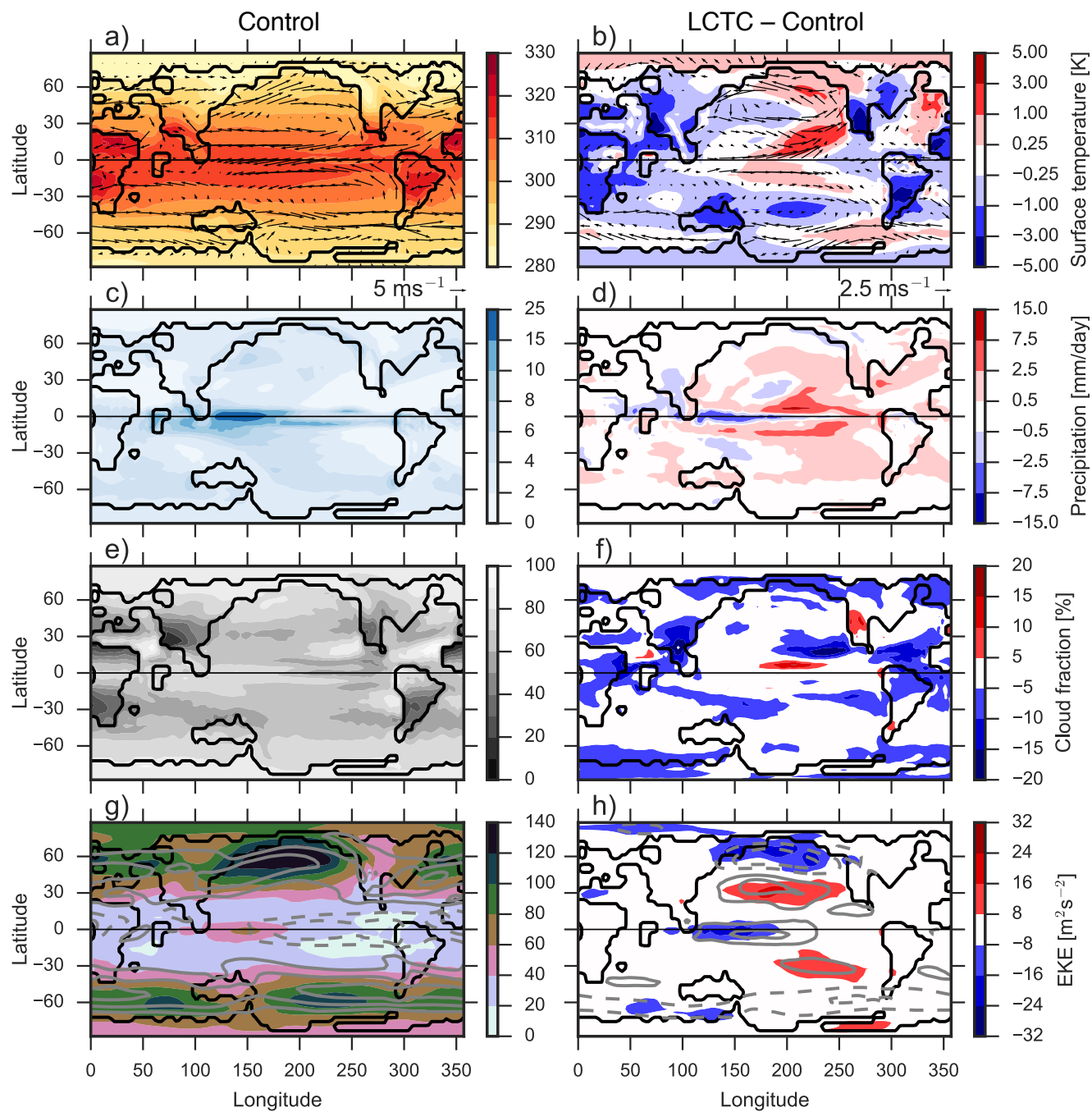


Figure 2. Annual-mean climatology in the control run (left column) and its change in the LCTC case (right column) of (a,b) surface temperature (shading) and 900 hPa wind (arrows); (c,d) precipitation; (e,f) cloud fraction and (g,h) eddy kinetic energy (shading) and zonal wind at 700 hPa (contours, c.i. 4 ms⁻¹ in (g) and 2 ms⁻¹ in (h)).

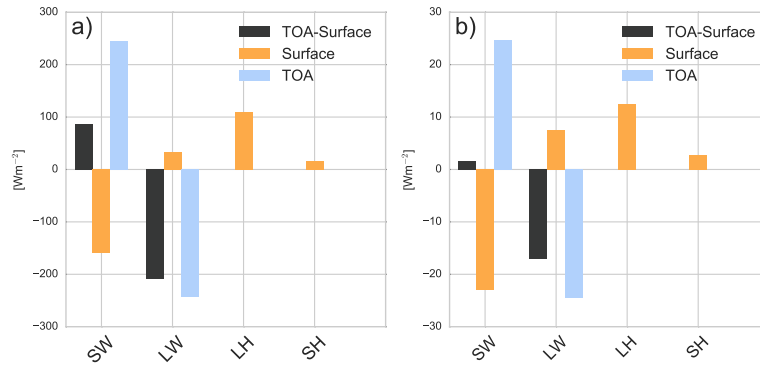


Figure 3. Terms in the global-mean atmospheric energy budget (Equation 2) for (a) the control simulation and (b) change in the LCTC case (LCTC – control).

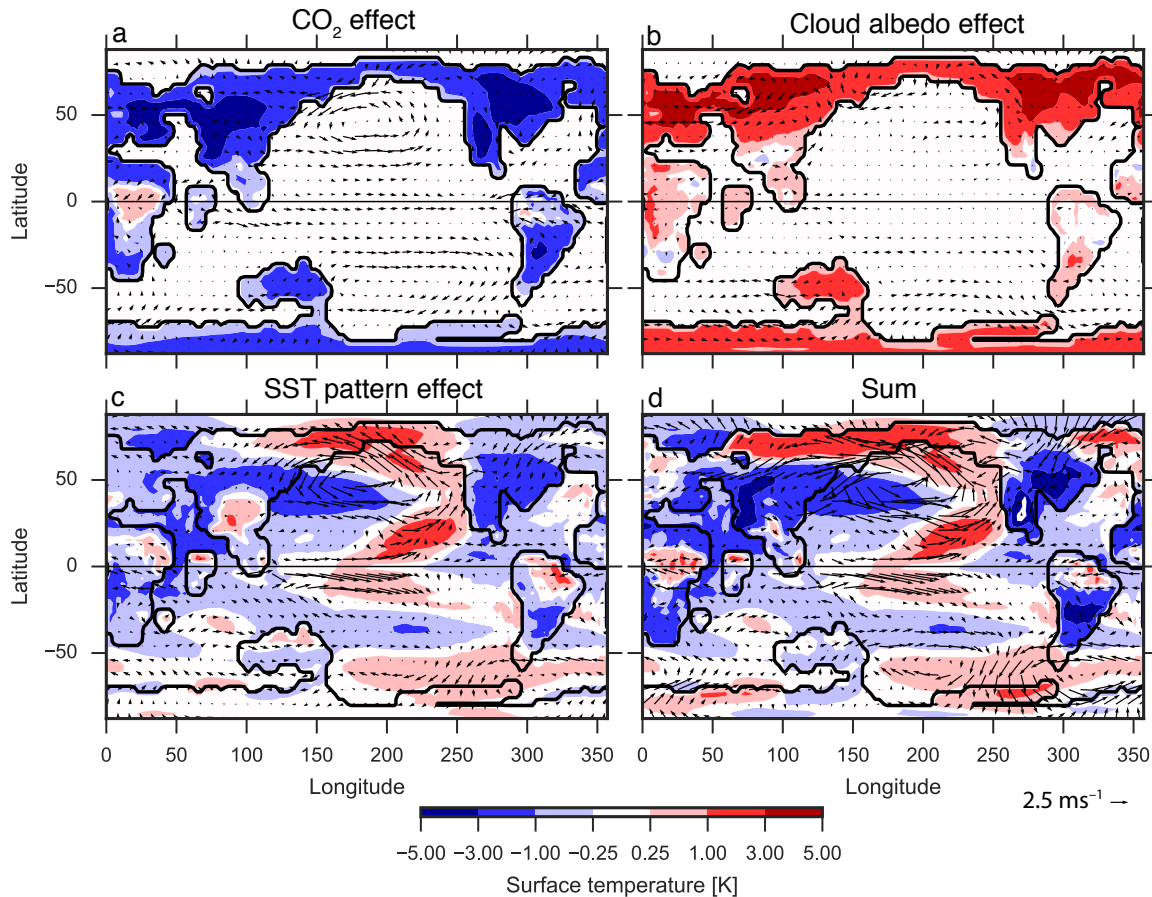


Figure 4. Change in annual-mean surface temperature (shading) and 900 hPa wind (arrows) between the control run and the fixed SST simulation with (a) reduced CO₂, (b) reduced cloud albedo and (c) change is SST pattern, as well as (d) the sum of all changes.

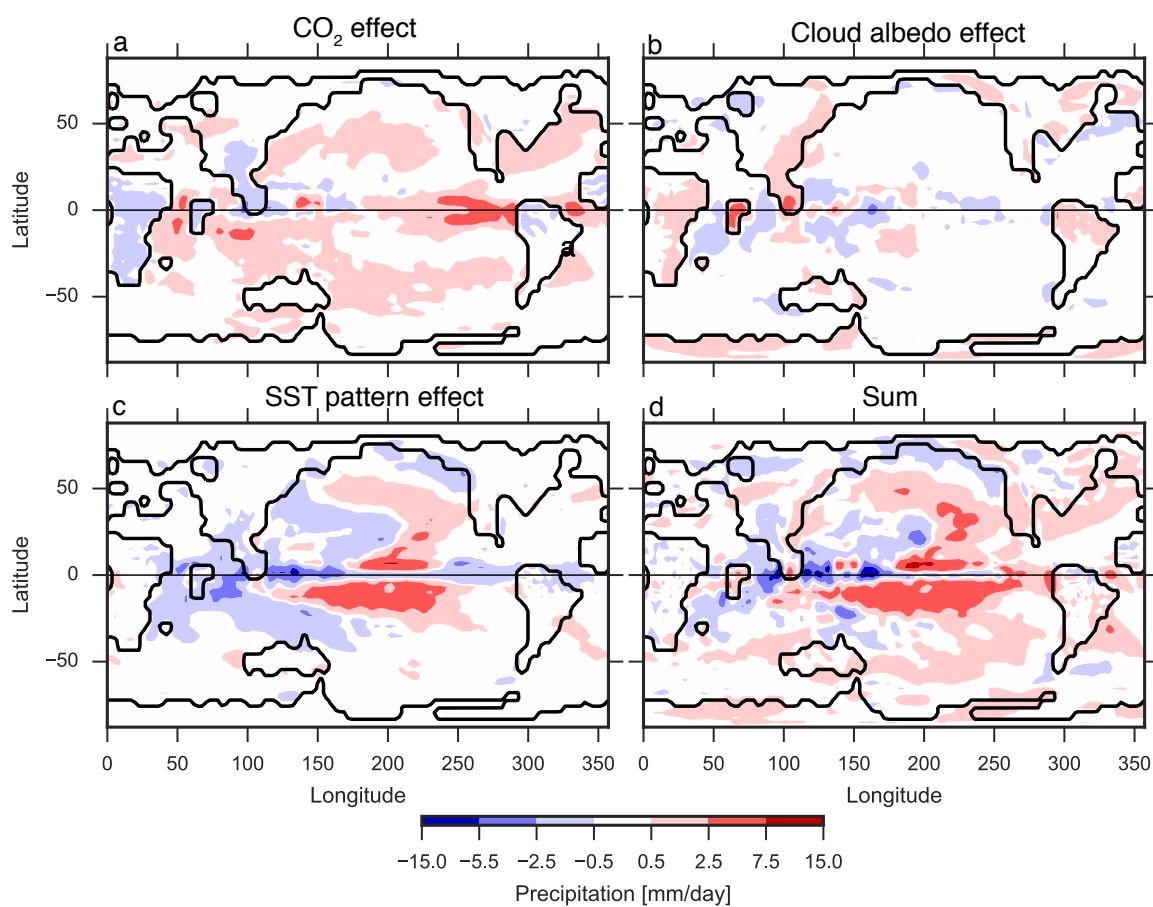


Figure 5. As in Figure 4 but for annual-mean precipitation.

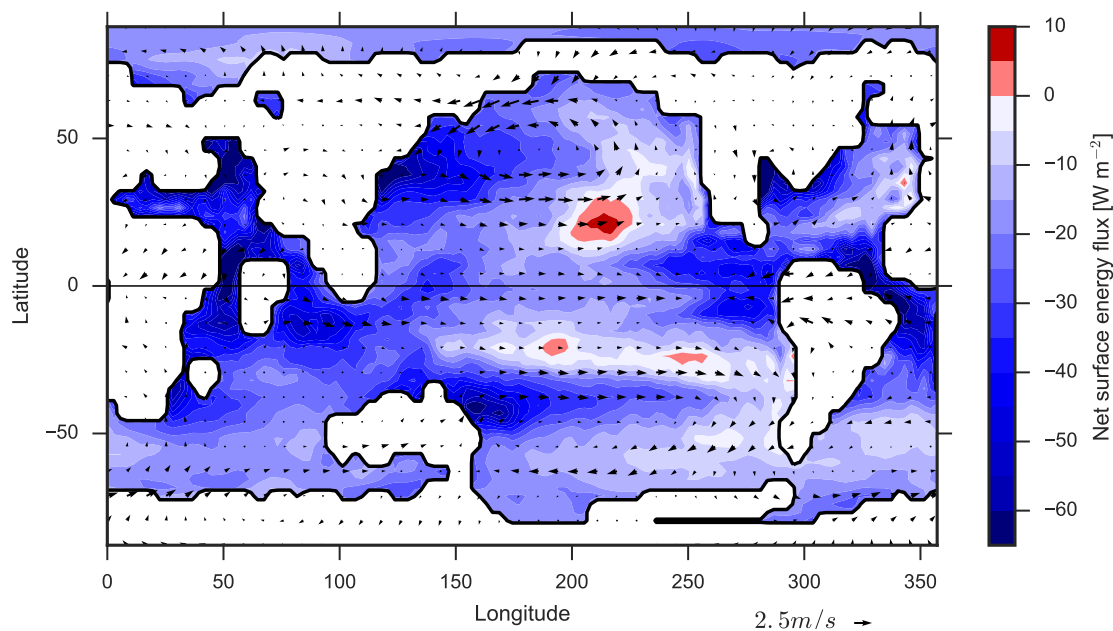


Figure 6. Change in annual-mean net surface energy flux (shading, defined positive downwards) and 900 hPa wind (arrows) between the control run and the fixed SST run with reduced CO_2 .

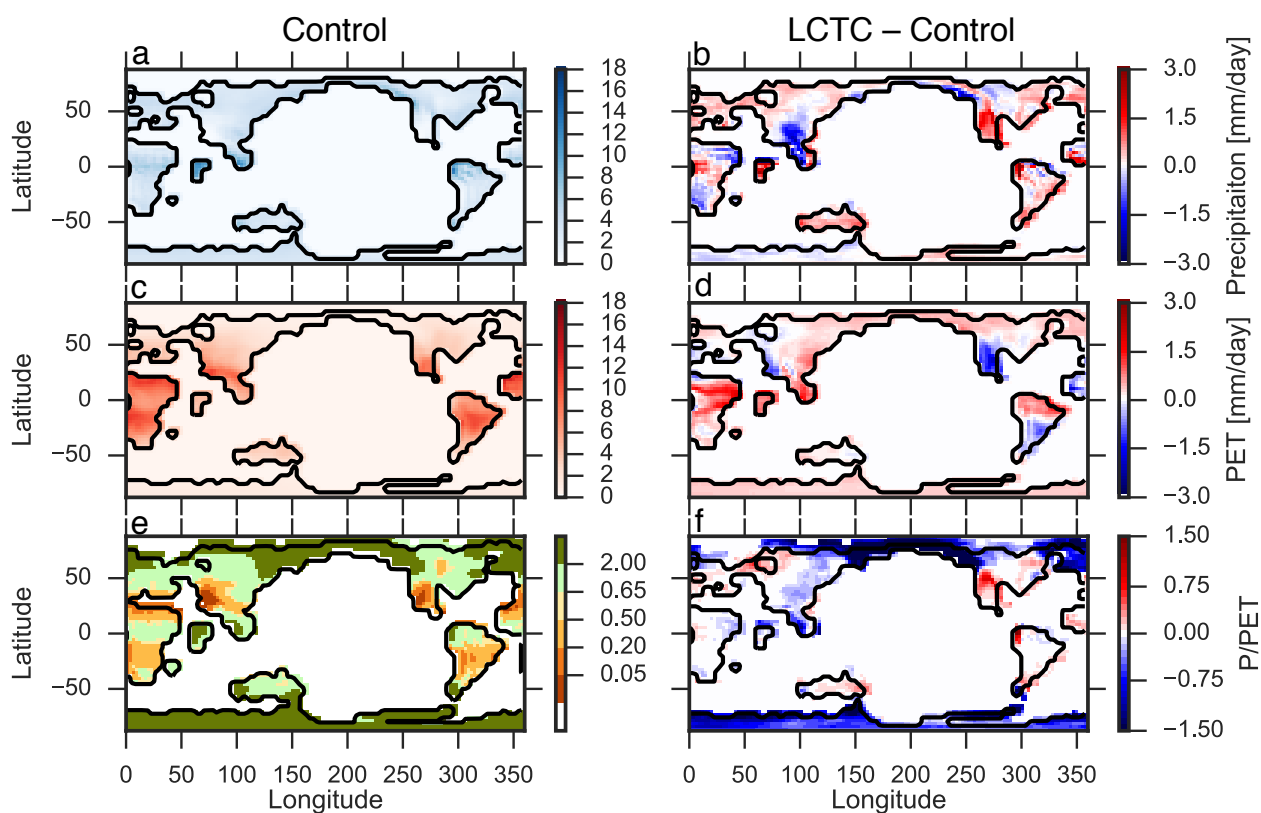


Figure 7. Annual-mean climatology over land areas only in the control run (left column) and change in the LCTC run (right column) of (a,b) precipitation P , (c,d) potential evapotranspiration PET and (e,f) the aridity index P/PET .